Simultaneous Design and Trajectory Optimization for Boosted Hypersonic Glide Vehicles

Jonathan R. Cangelosi* and Matthias Heinkenschloss[†] *Rice University, Houston, TX 77005, USA*

Jacob T. Needels[‡] and Juan J. Alonso[§] Stanford University, Stanford, CA 94305, USA

This manuscript describes a methodology for simultaneous vehicle and trajectory optimization of a hypersonic glide vehicle. The co-design problem is formulated as an optimization problem with constraints including vehicle dynamics, path constraints (e.g., surface heating), and other constraints. The discretized optimization problem is solved simultaneously in the vehicle design parameters, the state variables, and the controls using an interior point method. Gaussian process (GP) surrogates, which are generated from sample candidate designs and flight conditions, are used to model vehicle aerodynamic performance and mass properties, as well as their first and second-order derivatives required by the optimizer. These GP surrogates and their derivatives are computationally inexpensive, making the all-at-once optimization approach for the co-design problem more tractable. To mitigate the effect of surrogate model errors on the solution of the optimal control problem, the GP models are refined using samples of the vehicle aerodynamic performance and mass properties at the solution of the co-design problem with the current surrogate. The resulting framework is applied to maximizing the range of a hypersonic glide vehicle with path and terminal constraints. Possible extensions of this methodology are also discussed, including the incorporation of more complex vehicle models such as multi-fidelity models, as well as adaptive surrogate modeling strategies to mitigate the effect of model errors on the solution of the optimal control problem.

Nomenclature

A = vehicle aspect ratio design parameter

 A_w = reference area [m²]

B = vehicle shape design parameter

C = stagnation heating constant [kg^{0.5}/m^{1.5}]

 C_D = drag coefficient C_L = lift coefficient

 C_f = skin friction coefficient

D = drag force [kN]

g = gravitational acceleration [m/s²]

L = lift force [kN] l = kernel length scale ℓ = vehicle length [m] Ma = Mach number m = mass [kg]

N = number of samples

n = planform shape design parameter

P = pressure [kPa]

^{*}Ph.D. Candidate, Rice University, Department of Computational Applied Mathematics and Operations Research.

[†]Noah Harding Chair and Professor, Rice University, Department of Computational Applied Mathematics and Operations Research.

[‡]Ph.D. Candidate, Stanford University, Department of Aeronautics and Astronautics, AIAA Student Member.

[§]Vance D. and Arlene C. Coffman Professor, Stanford University, Department of Aeronautics and Astronautics, AIAA Fellow.

 $\dot{Q}_{
m stag}$ stagnation point heat rate [MW/m²] dynamic pressure [kPa] R_E radius of Earth [km] Reynolds number Re Ttemperature [K] flight duration [s] t_f velocity magnitude [km/s] x, y, zCartesian position [km] angle of attack [rad] wave angle [rad] β flight path angle [rad] γ δ flow turning angle [rad]

 θ = vehicle centerline wedge angle [rad]

 κ = specific heat ratio μ = dynamic viscosity [Pa-s] μ_d = vehicle design parameter vector μ_g = gravitational parameter [m³/s²] ν = Prandtl-Meyer function [rad] ρ = atmospheric density [kg/m³]

Subscripts

e = quantity evaluated at boundary layer edge

l = lowerp = planform

u = upper

w =quantity evaluated at wall

 ∞ = free-stream quantity

I. Introduction

HYPERSONIC vehicle design and optimization is challenging due to unique physical effects at high speeds, which result in strong, nonlinear coupling between vehicle systems and necessitate an integrated, multidisciplinary approach to design [1]. Particular challenges of hypersonic flight include aerodynamic performance due to shock-dominated flow fields, the coupling of the boundary and thermal layers and large wave drag, and extreme thermal loads and surface temperatures due to aerodynamic heating. Aerodynamic performance and aerothermal environments are strongly dependent on flight conditions and therefore the vehicle trajectory must be included in analysis and optimization.

This manuscript focuses on boosted hypersonic glide vehicles, a class of hypersonic aircraft that are launched to high altitude on a rocket or other launch system and glide unpowered at high speed to the ground [2]. Because they have no onboard propulsion system, these vehicles must balance glide aerodynamic efficiency against competing requirements during the initial dive, including sufficient lift and drag force to decelerate as well as thermal protection system (TPS) mass to accommodate heating loads.

In the literature, there is significant work on optimization of hypersonic vehicle systems, employing methods of varying fidelity and different levels of integration between trajectory and vehicle optimization. In [3], trajectory optimization for boosted hypersonic glide vehicles is studied, employing pseudospectral methods to develop detailed control models through the full trajectory, utilizing polynomial surrogates to model aerodynamic properties as a function of attitude for fixed vehicle configurations. In [4], structural and TPS parameters are simultaneously optimized along with a control schedule discretized into several segments for a fixed aerodynamic database. In [5], both vehicle geometry and equilibrium altitude are modified to perform a multi-objective optimization of vehicles for aero-gravity assist maneuvers. The paper [6] computes desensitized controls, i.e., state and control sensitivities with respect to a few problem parameters, are included in the formulation of the trajectory optimization problem to reduce sensitivity of optimal trajectories to variations in these problem parameters [7]. The work [8] accounts for a possible mismatch between the model dynamics used for trajectory optimization and the true vehicle dynamics using an iterative model update in which the current model is updated using a specific model parameterization to reduce the mismatch between the optimal trajectory

computed with the current model and the trajectory obtained by applying the computed optimal control to a high-fidelity vehicle simulator that uses feedback control mechanisms to track the prescribed trajectory. Frameworks for high-fidelity vehicle-trajectory optimization have been described in the literature, including a method for multidisciplinary analysis and optimization for an air-breathing hypersonic aircraft that improves propulsion, aerodynamic, aerothermal, structural, and trajectory performance using an iteratively refined surrogate model [9]. A key challenge of the simultaneous design problem is including disciplinary simulation data in the optimization process. Both [4] and [9] describe the use of surrogate models to characterize performance over the design space. The resulting optimization problem is then solved using iterative procedures in which candidate designs are sequentially evaluated for optimal trajectory performance.

In this work, we focus on a combined vehicle design and trajectory optimization problem, referred to in this paper as a co-design problem. Computationally expensive model components such as lift and drag coefficients are approximated by computationally inexpensive twice-differentiable surrogates. As a result, the co-design problem becomes tractable by an all-at-once approach where an appropriate discretization of the constrained optimization problem is solved simultaneously for the vehicle parameters, states, and controls using a suitable, fast, (first- and second-order) derivative-based nonlinear optimization algorithm. Compared to other optimization approaches, the all-at-once approach makes use of the entire optimization problem, enabling more efficient exploration of the combined design parameters, state, and control space, typically resulting in faster convergence. Moreover, this approach allows the user to easily adjust the co-design problem formulation, e.g., by adding constraints, without significant implementation burden.

Given a surrogate, we use a primal-dual interior point method to solve a Radau collocation-based discretization of the co-design problem. This will be explained in more detail in Sect. II. We use Gaussian process (GP) models to compute computationally inexpensive surrogates of model component functions from samples of the underlying true functions. Analytical first- and second-order derivatives are easily computed for GP models at low computational cost [10], making them well suited for derivative-based optimization. Details will be provided in Sect. IV. Since the quality of the GP surrogates impacts the quality of the computed vehicle design and trajectory, we use a sequence of GP surrogates computed with additional samples to assess and improve the quality of the computed solution in Sect. V.B. The solution of the optimization problem computed using a given GP surrogate is used as the initial iterate for the solution of the optimization problem using the next refined GP surrogate, thus improving the overall efficiency of our approach.

This manuscript is organized as follows: Sect. II provides an overview of the combined vehicle-trajectory optimization problem and the numerical solution method used in this work. Sect. III describes the parametric vehicle geometry, as well as the physical models for aerodynamic analysis, aerothermal modeling, weight estimation, and vehicle dynamics. The GP surrogate models used are described in Sect. IV. In Sect. V, optimization results are presented for the dive and glide phases of a boosted hypersonic glide vehicle, and a preliminary model refinement approach is applied to iteratively improve the solution. Finally, the manuscript concludes with a discussion of future work, including the incorporation of additional physical models and constraints, the addition of multi-fidelity data, and more sophisticated methods for surrogate model refinement.

II. Coupled Vehicle-Trajectory Optimization

The simultaneous vehicle-trajectory optimization is expressed compactly as an optimization problem of the following form:

$$\min_{\boldsymbol{\mu}_{d}, \mathbf{x}(\cdot), \mathbf{u}(\cdot), t_{f}} \quad \phi(\boldsymbol{\mu}_{d}, \mathbf{x}(t_{f}), t_{f}) + \int_{0}^{t_{f}} f_{0}(\boldsymbol{\mu}_{d}, \mathbf{x}(t), \mathbf{u}(t), t) dt,$$
s.t.
$$\frac{d}{dt} \mathbf{x}(t) - \mathbf{f}(\boldsymbol{\mu}_{d}, \mathbf{x}(t), \mathbf{u}(t), t) = \mathbf{0}, \qquad t \in [0, t_{f}],$$

$$\mathbf{b}(\boldsymbol{\mu}_{d}, \mathbf{x}(0), \mathbf{x}(t_{f}), t_{f}) \leq \mathbf{0},$$

$$\mathbf{g}(\boldsymbol{\mu}_{d}, \mathbf{x}(t), \mathbf{u}(t), t) \leq \mathbf{0}, \qquad t \in [0, t_{f}],$$
(1)

where ϕ is a terminal objective functional associated with vehicle performance and design for a given mission (e.g., maximum downrange, minimum volume), f_0 is a running objective functional, \mathbf{f} represents the equations of motion that guide the dynamics of the vehicle expressed as a first-order ODE, \mathbf{b} denotes a set of initial and terminal conditions, and \mathbf{g} represents time-dependent mixed control-state constraints (also called path constraints). The vectors $\mathbf{x}(t) \in \mathbb{R}^n$ and $\mathbf{u}(t) \in \mathbb{R}^m$ represent the vehicle states and controls, respectively, at time t, and $\mu_d \in \mathbb{R}^k$ is a vector of parameters representing vehicle design variables.

In many problems, e.g., when downrange is maximized, the flight duration t_f is determined as part of the solution to the optimization problem and therefore is included in Eq. (1) as an optimization variable. These free-time, finite-horizon problems are easily handled by changing time to $t \mapsto t_f \cdot \tau$ for $\tau \in [0, 1]$, scaling the dynamic equations appropriately by t_f , and solving the resulting fixed-time problem with $\tau \in [0, 1]$. Additional constraints could be added to Eq. (1) for greater complexity.

One significant advantage of this simultaneous vehicle-trajectory optimization formulation is its flexibility. By incorporating dependence on vehicle parameters in the optimal control problem, we can tailor a vehicle's design to its mission objective, effectively coupling vehicle design and trajectory optimization. Additionally, while certain vehicle configurations may only yield infeasible trajectories (e.g., due to insufficient thermal protection), adjusting the vehicle parameters may yet yield feasible ones. In other words, this problem which includes vehicle parameters μ_d as optimization variables is more likely to be feasible than a typical trajectory optimization problem where the parameters μ_d are fixed and the constraints of the problem may need to be adjusted to obtain a solution. However, other formulations may be considered; for instance, rather than being restricted to optimizing a single objective function, one may wish to balance multiple competing goals (e.g., minimize the weight of the TPS and maximize downrange) by solving a multi-objective optimization problem, where one seeks Pareto-optimal solutions rather than optimal solutions. Such an approach is outside the scope of this paper.

Incorporating both vehicle design and control within a single optimization process has been demonstrated in the literature, e.g., in [11], and several methods exist to perform the joint optimization [12]. For example, one could perform trajectory optimization in the inner loop of an optimizer with vehicle design optimization in the outer loop, which could be accomplished efficiently using surrogate optimization techniques. However, one can also solve Eq. (1) all-at-once, i.e., solve Eq. (1) as a constrained optimization problem with optimization variables given by the parameters μ_d and t_f , states \mathbf{x} , and controls \mathbf{u} . This approach is used in this work for reasons discussed in Sect. I.

Specifically, we use a so-called direct method (see, e.g., [13], [14, Sec. 4.5], [15, Ch. 10]) with a Radau collocation-based discretization of the dynamics and constraints in Eq. (1) and a compatible quadrature for the integral term in the objective in Eq. (1). This discretization scheme belongs to the class of pseudospectral collocation methods, which are frequently used in trajectory optimization and other applications. This discretization scheme has several advantages, including good numerical stability properties [15, p. 293], availability of discretization error analyses for the optimal control problem Eq. (1) without path inequality constraints [15, Sec. 10.4], [16], [17], and the ability to map the Lagrange multipliers of the nonlinear programming problem (NLP) that arises from the Radau collocation-based discretization of Eq. (1) to the co-states of the infinite-dimensional problem [18], [16]. The direct method, i.e., using discretization to transcribe Eq. (1) into an NLP, has several advantages in our application, particularly ease of handling path inequality constraints and possibly other constraints. See, e.g., [19] and [13] or [14, Sec. 4.5] for detailed discussion of direct method vs. so-called indirect methods.

As mentioned previously, the Radau collocation-based discretization of Eq. (1) leads to a transcription of the infinite-dimensional problem into an NLP. We assume that the functions ϕ , f_0 , f, g, g are twice continuously differentiable. This implies that objective and constraint functions in the NLP are twice continuously differentiable, and we use an optimization algorithm that makes use of this second-order derivative information. Specifically, we use the primal-dual interior point method Ipopt [20], which is freely available from https://coin-or.github.io/Ipopt, to solve this NLP. Additional details on the discretization and initialization strategies for the NLP solver will be given in Sect. V. We use algorithmic differentiation [21], specifically the jax library, https://jax.readthedocs.io, to compute first-and second-order derivatives of ϕ , f_0 , f, g, and g.

In the co-design problem, the dynamics **f** depend on aerodynamic force coefficients that are typically expensive to compute in high fidelity. Other constraints (e.g., heating constraints) may also depend on functions that are expensive to evaluate, but to focus our presentation we only consider the dependence of the dynamics **f** on expensive-to-evaluate aerodynamic force coefficients. Since the numerical solution of Eq. (1) requires many evaluations of these expensive coefficient functions, direct use of the computationally expensive high-fidelity models may result in unacceptably long run times of the optimization algorithm. To perform the optimization in a computationally tractable manner, we use efficient-to-evaluate surrogate models with appropriate approximation quality. To highlight the dependence of the dynamics **f** on expensive-to-evaluate aerodynamic force coefficients or surrogates thereof, we write dynamics as

$$\mathbf{f}(\mathbf{p}(\mu_d, \mathbf{x}(t), \mathbf{u}(t)), \mu_d, \mathbf{x}(t), \mathbf{u}(t), t),$$

where $\mathbf{p}: \mathcal{P} \times \mathcal{X} \times \mathcal{U} \mapsto \mathbb{R}^l$ is the function that maps a given point in the joint parameter \mathcal{P} , state \mathcal{X} , and control space \mathcal{U} to the aerodynamic force coefficients or surrogates thereof. We use \mathbf{p}_* to denote the computationally expensive

high-fidelity evaluation of the aerodynamic force coefficients and $\hat{\mathbf{p}}$ to denote a computationally inexpensive surrogate. With this in mind, we reformulate Eq. (1) to incorporate these additional dependencies explicitly as

$$\min_{\substack{\mu_{d}, \mathbf{x}(\cdot), \mathbf{u}(\cdot), t_{f}}} \quad \phi(\mu_{d}, \mathbf{x}(t_{f}), t_{f}) + \int_{0}^{t_{f}} f_{0}(\mu_{d}, \mathbf{x}(t), \mathbf{u}(t), t) dt,$$
s.t.
$$\frac{d}{dt} \mathbf{x}(t) - \mathbf{f} \Big(\mathbf{p} \big(\mu_{d}, \mathbf{x}(t), \mathbf{u}(t) \big), \mu_{d}, \mathbf{x}(t), \mathbf{u}(t), t \Big) = \mathbf{0}, \quad t \in [0, t_{f}],$$

$$\mathbf{b} \big(\mu_{d}, \mathbf{x}(0), \mathbf{x}(t_{f}), t_{f} \big) \leq \mathbf{0},$$

$$\mathbf{g} \big(\mu_{d}, \mathbf{x}(t), \mathbf{u}(t), t \big) \leq \mathbf{0}, \quad t \in [0, t_{f}],$$
(2)

where $\mathbf{p} = \hat{\mathbf{p}}$ when a surrogate is used. The direct method described earlier for Eq. (1) can easily be applied to Eq. (2). We assume that the surrogates $\hat{\mathbf{p}}$ are twice continuously differentiable, which together with our previous differentiability assumptions on ϕ , f_0 , \mathbf{f} , \mathbf{g} , and \mathbf{b} implies that objective and constraint functions in the resulting NLP are twice continuously differentiable; thus, Ipopt or any other suitable optimization algorithm can be applied.

Note that surrogate quality will influence the quality of the solution. Fundamentally, we seek the solution of Eq. (2) with $\mathbf{p} = \mathbf{p}_*$, but are unable to do so directly at reasonable computational expense. Provided $\hat{\mathbf{p}}$ is a suitable approximation of \mathbf{p}_* , which is itself an accurate model of the underlying physical mechanisms governing vehicular motion, the optimal solution of Eq. (2) will be reflective of the "real-world" solution. To achieve this "real-world" fidelity, we may refine the surrogate models using a collection of sample evaluations of \mathbf{p}_* , which has a modest computational cost compared to solving Eq. (2) directly with $\mathbf{p} = \mathbf{p}_*$. In this paper, we use a simple strategy for GP refinement, and more sophisticated strategies for adaptive surrogate refinement will be discussed in future work.

Next, we specify our vehicle model and our specific vehicle-trajectory optimization problem.

III. Vehicle Model

This study employs a parametric hypersonic waverider vehicle model adapted from [5, 22]. The geometry is defined by the parameter set $\{A, n, \ell, \theta, Ma_d\}$ where A and n are shape parameters, ℓ is the vehicle axial length, θ is the vehicle centerline wedge angle, and Ma_d is a design Mach number used to specify the surface curvature. For a specified value of Ma_d , the wedge angle θ of the vehicle implies a shock angle β which can be determined by solving the oblique shock relations. The vehicle planform is the same for both upper and lower surfaces, with the leading edge on the vehicle axis of symmetry located at the origin. The axial domain of both surfaces has the extent $x \in [0, \ell]$. The vehicle planform is defined by the power law relation

$$y_p = Ax^n$$
,

which is mirrored across the y-axis to obtain the full symmetric geometry. The z-position of each point in the domain bounded by the axial extent of the vehicle and the planform boundary can then be evaluated as

$$z_u = (y_u/B)^{1/n}$$

for the upper surface and

$$z_l = x_l \tan \theta + (y_l/A)^{1/n} (\tan \beta - \tan \theta)$$

for the lower surface. To enforce consistency in the leading edge of the upper and lower surfaces, the parameter B is solved as

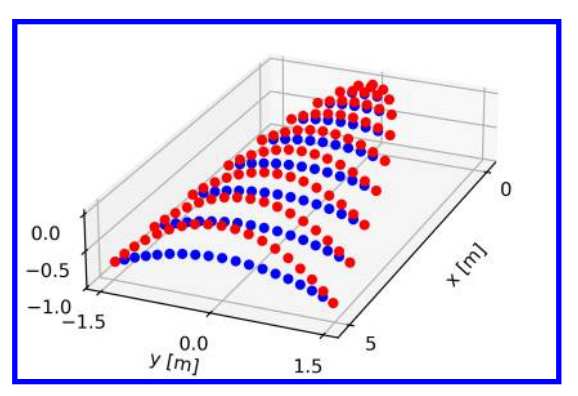
$$B = \frac{A}{\tan^n \beta}.$$

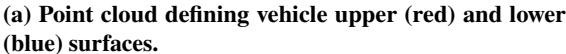
An example vehicle geometry with A = 0.66, n = 0.5, $\ell = 5$ m, $Ma_d = 12$, and $\theta = 5^{\circ}$ is shown in Figs. 1a-1b. In principle, the aspect ratio A, the parameter n which controls the shape of the planform boundary, and the vehicle axial length ℓ may be included as design parameters for optimization, but fixed values

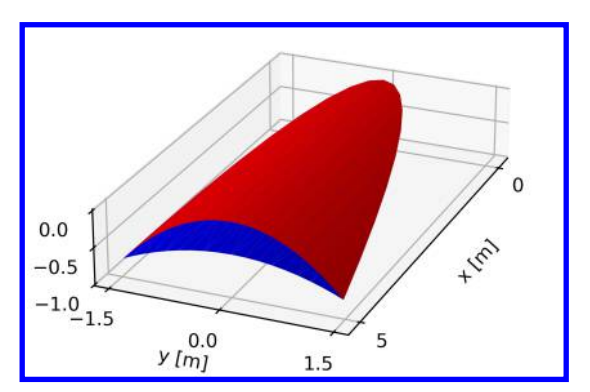
$$A = 0.6, \quad n = 0.5, \quad \ell = 5 \text{ m}$$
 (3)

are used in this study. Thus, the vehicle design parameters to be optimized are the design Mach number Ma_d and the wedge angle θ , i.e.

$$\mu_d = [Ma_d, \theta]^{\mathsf{T}}.$$







(b) Surface grid generated through Delaunay triangulation of point cloud.

Fig. 1 Illustration of example parametric waverider geometry.

A. Aerodynamic Model

The parametric vehicle analysis code SHARPE [23] is used to compute mass and aerodynamic properties. As shown in Fig. 1b, the upper and lower surfaces of the vehicle surface grid are triangulated using a Delaunay algorithm to obtain a set of discrete panels. Aerodynamic relations described below are used to solve for the pressure and viscous forces on each panel, which are then used to determine the overall aerodynamic forces and force coefficients on the vehicle for a given flight condition. For the vehicle geometries considered in this study, the vehicle is generated so that, at the design condition, a planar shock is attached at the leading edge.

Under the assumption of a planar shock wave attached to the vehicle edge, the pressure on the vehicle lower surface panels is equal to the post-shock static pressure of the oblique shock. This provides an accurate approximation of surface pressure at or near the vehicle design point, but becomes less accurate away from the design point where the approximation of a planar shock is less accurate. An oblique shock method, where the flow deflection angle δ is given by the vehicle wedge angle and the vehicle angle of attack, is used to determine the boundary layer edge conditions for the compression surface. The wave angle β can then be determined by solving the implicit relation

$$\cot \delta = \tan \beta \left[\frac{(\kappa + 1)Ma^2}{2(Ma^2 \sin^2 \beta - 1)} - 1 \right].$$

Given the wave angle, oblique shock relations can then be used to determine the post-shock static pressure, temperature, and velocity. On the expansion surface of the vehicle, the Prandtl-Meyer function is used to determine boundary layer edge properties. The turning angle of the flow is calculated in a similar manner to the shock deflection angle and is used to determine the change in Mach number through the expansion using the Prandtl-Meyer function

$$\nu(Ma_2) = \nu(Ma_1) + \delta,$$

where

$$\nu(Ma) = \int \frac{\sqrt{Ma^2-1}}{1+\frac{\kappa-1}{2}Ma^2} \frac{dMa}{Ma}.$$

Given the post-expansion Mach number, isentropic relations can be used to compute the post-expansion properties. For small angle of attack, the base of the vehicle remains completely shadowed, and an empirical value for the recovered pressure of $0.45P_{\infty}$ is used [5]. Viscous drag is computed for the acreage surface of the vehicle assuming a laminar compressible boundary layer using the Eckert reference temperature method [24], as described in [25]. Boundary layer edge properties are determined from the inviscid flowfield solution for the compression and expansion methods described previously. The local skin friction coefficient is computed as

$$C_f = \frac{0.664\sqrt{CR(T^*)}}{\sqrt{Re_x}},$$

where $CR(T^*)$ is the Chapman-Rubesin parameter

$$CR(T^*) = (T^*/T_e)^{-1/3}$$

evaluated at the Eckert reference temperature

$$\frac{T^*}{T_e} = 0.5 + 0.039 Ma_e^2 + 0.5 \frac{T_w}{T_e}.$$

The local Reynolds number Re_x is evaluated as

$$Re_x = \frac{\rho_e v_e x_{LE}}{\mu_e},$$

where x_{LE} is computed as the distance from the leading edge to a surface panel centroid and μ_e is the dynamic viscosity, which is computed using Sutherland's law [26] based on the temperature at the boundary layer edge as

$$\mu(T) = 1.458 \times 10^{-6} \frac{T^{3/2}}{T + 110.4}.$$

For this study, aerodynamic forces are computed for a single, fixed altitude, so that force coefficients are only a function of angle of attack and velocity. This reduces the dimension of the surrogates for this work, though in principle altitude could be added as an additional dependency. A fixed altitude of 60 km was selected to compute aerodynamic properties since it is representative of much of the dive and glide phases of flight, which are the primary modeling focus of this work. There are significant aerodynamic effects that occur in both high- and low-altitude flows which are not captured in the aerodynamic models used in this study, such as rarefaction [27] and turbulent transition [28], which motivate the use of a multi-fidelity approach in a future study incorporating altitude as a variable.

B. Weight Estimation

In order to compare relative performance of candidate designs, a vehicle weight estimation model is required to assess the impact of modifying design parameters on vehicle mass. Vehicle mass is estimated using a notional structural model layout; while incorporating detailed structural analysis and sizing is beyond the scope of this work, estimated structural component sizes are used to generate a first-principles mass buildup for each given configuration. Given vehicle parameters $\mu_d = [Ma_d, \theta]^{\top}$ we compute the mass $m(Ma_d, \theta)$ of the vehicle as the sum of individual contributions

$$m(Ma_d, \theta) = m_{\text{struct}}(Ma_d, \theta) + m_{\text{TPS}}(Ma_d, \theta) + m_{\text{subsys}} + m_{\text{payload}}.$$
 (4)

Table 1 lists the dimension and material of each major vehicle structural component. In Eq. (4), $m_{\text{struct}}(Ma_d, \theta)$ is the structural mass contribution from the vehicle skin, frames, and stringers, and $m_{\text{TPS}}(Ma_d, \theta)$ is the mass of the TPS. The vehicle skin is assumed to have constant thickness over the entire surface area. Bulkhead-forming members are employed starting from the rear surface of the vehicle at equidistant locations along the vehicle axial position. Stringers are employed along the vehicle leading edge and at two additional spanwise positions along the vehicle semi-span to stiffen the skin against panel buckling and transfer load from the vehicle skin to the frame. The vehicle structural layout is illustrated schematically in Fig. 2.

Component	Dimension	Material	Density [kg/m ³]
Skin	7.5 mm thick	Titanium 6A1-4V [29]	4437.5
Acreage TPS	5 cm thick	AETB-12 Si-based ceramic tile [30]	192.0
Leading Edge TPS	5 mm along LE radius	Reinforced carbon/carbon [25]	1656.3
Stringers	1 cm ² , varying length	Aluminum 2024-T4 [31]	2780.0
Frames	5×1 cm thick, 50% infill	Aluminum 2024-T4	2780.0
Subsystems	Fixed mass of 100 kg	_	_
Payload	Fixed mass of 150 kg	_	_

Table 1 Summary of components and materials for vehicle structural and weight model.

To calculate $m_{TPS}(Ma_d, \theta)$, we assume the vehicle acreage surface to be covered in a constant-thickness TPS. Since heat loads are highest along the vehicle leading edge, a reinforced carbon-carbon TPS is employed in this region, sized

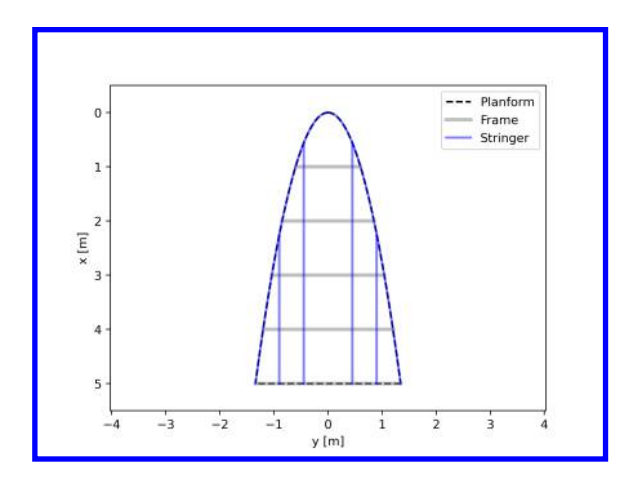


Fig. 2 Planform view of vehicle structural components.

to cover the vehicle leading edge radius along the entire arc length of the vehicle planform. The constant TPS sizing in this study is an approximation since thermal loads vary significantly over the vehicle surface. Future work could incorporate TPS sizing over different regions of the vehicle surface as additional design variables and aim to minimize mass for spatially varying thermal loads. In this sense, we expect the mass of the vehicle to be overestimated compared to an as-built mass.

C. Vehicle Dynamics

The atmospheric density model used in this work is an exponential fit of the Standard Atmosphere and is given by

$$\rho(y) = 1.225e^{-0.14y}$$

The dynamic pressure is given by

$$\bar{q}(y,v) = \frac{1}{2}\rho(y) v^2.$$
 (5)

The lift and drag forces are given by

$$L(y, v, \alpha, Ma_d, \theta) = \bar{q}(y, v) C_L(v, \alpha, Ma_d, \theta) A_w,$$
(6a)

$$D(y, v, \alpha, Ma_d, \theta) = \bar{q}(y, v) C_D(v, \alpha, Ma_d, \theta) A_w.$$
(6b)

The reference area $A_w \approx 8.91 \text{ m}^2$ was determined from the fixed vehicle parameters in Eq. (3) by taking the planform area of the resulting geometry. Since neither of the design parameters considered in this study affect the planform area of the vehicle, the reference area of the vehicle is fixed in our setting. The lift and drag coefficients $C_L(v, \alpha, Ma_d, \theta)$ and $C_D(v, \alpha, Ma_d, \theta)$ depend on the velocity v, angle of attack α , and vehicle design parameters $\mu_d = [Ma_d, \theta]^{\top}$. Throughout the trajectory, the angle of attack α was assumed to be commanded within appropriate limits, and the existence of a control system that produces the necessary control moments was assumed, though not explicitly modeled in the vehicle geometry. We constructed GP surrogate models for these coefficients using samples of lift and drag coefficients computed using SHARPE. The lift and drag forces were computed by summing the pressure and viscous forces on each panel of the discretized vehicle geometry, which was then normalized by the reference area and flight condition dynamic pressure to obtain C_L and C_D .

A vehicle dynamic model is adapted from [32] with zero thrust and bank angle, given as

$$\begin{bmatrix} \frac{d}{dt}x\\ \frac{d}{dt}y\\ \frac{d}{dt}y\\ \frac{d}{dt}\gamma \end{bmatrix} = \begin{bmatrix} v\cos\gamma\\ v\sin\gamma\\ -\frac{1}{m(Ma_d,\theta)} \left(D(y,v,\alpha,Ma_d,\theta) + m(Ma_d,\theta)g(y)\sin\gamma\right)\\ \frac{1}{m(Ma_d,\theta)v} \left(L(y,v,\alpha,Ma_d,\theta) - m(Ma_d,\theta)g(y)\cos\gamma + \frac{m(Ma_d,\theta)v^2\cos\gamma}{R_E+y}\right) \end{bmatrix}, \quad t \in [0,t_f], \quad (7)$$

with state vector $\mathbf{x}(t) = [x(t), y(t), v(t), \gamma(t)]^{\mathsf{T}}$, control input $\mathbf{u}(t) = \alpha(t)$, and vehicle parameters $\mu_d = [Ma_d, \theta]^{\mathsf{T}}$. Gravitational acceleration g is computed as a function of altitude y by the inverse-square law:

$$g(y) = \frac{\mu_g}{(R_E + y)^2},$$

where $\mu_g = 3.986 \times 10^{14} \text{ m}^3/\text{s}^2$ is the standard gravitational parameter and $R_E \approx 6371 \text{ km}$ is the radius of Earth.

D. Aerothermal Model

Heating is generally maximal at the vehicle stagnation point, making that an appropriate location to assess aerothermal loads on the vehicle. Stagnation point heating is modeled using a correlation for a swept cylinder given in [33]. At the vehicle stagnation point, the sweep angle is zero and we can make a conservative approximation of heating by assuming a cold wall ($h_w \ll H_\infty$), which gives the relation

$$\dot{Q}_{\text{stag}}(y, v) = C\rho(y)^{0.5}v^3,$$

where a fixed leading edge radius of $R_n = 12$ mm is used, yielding a value of $C \approx 1.18 \times 10^{-3} \text{ kg}^{0.5}/\text{m}^{1.5}$ according to [33, Eq. 41].

IV. Gaussian Process Surrogate Models

In this work, we use GP surrogate models of mass $m(Ma_d, \theta)$ defined in Eq. (4), and of lift and drag coefficients $C_L(v, \alpha, Ma_d, \theta)$, $C_D(v, \alpha, Ma_d, \theta)$ defined in Eq. (6). GP regression, also known as kriging, can be used to model the outputs of an unknown function as a collection of jointly distributed Gaussian random variables given a set of function evaluations. We summarize the process of GP regression for a generic scalar-valued function f depending on a generic vector f. In our application, f is one of the functions f0 and the input is f1 is f2 or f3 and f4 is an appropriate.

A GP uses sample points $X = [x_1, ..., x_N]^{\top}$, corresponding observations $Y = [y_1, ..., y_N]^{\top}$ of f(x), and a kernel k to determine a predicted value y_* of f at an unsampled point x_* . The joint prior distribution of the training data Y and the test output y_* is, assuming zero mean,

$$\begin{pmatrix} Y \\ y_* \end{pmatrix} \sim \mathcal{N} \left(\mathbf{0}, \begin{bmatrix} k(X, X) + \sigma_n^2 \mathbf{I} & k(X, x_*) \\ k(x_*, X) & k(x_*, x_*) \end{bmatrix} \right), \tag{8}$$

where for $X_1, X_2 \subset X$ we use the notation $k(X_1, X_2)$ to denote the matrix of pairwise evaluations of the kernel k at the locations given by $X_1 \times X_2$, and σ_n^2 is a noise parameter that is used either to improve conditioning or to incorporate measurement uncertainty into the model [10]. In this work the radial basis function (RBF) kernel

$$k(x, x') = \sigma_f^2 \exp\left(\frac{-\|x - x'\|^2}{2l^2}\right)$$
 (9)

is used, where σ_f^2 is a hyperparameter that affects the amplitude of the model function and l is a lengthscale hyperparameter that determines how oscillatory the model function is. Using Eq. (8), the mean and variance of the prediction y_* for the unknown value $f_*(x_*)$ can be determined from the conditional probability distribution of the predicted values conditioned on the training data and sampling point as

$$y_*|X, Y, x_* \sim \mathcal{N}(\bar{y}_*, \text{var}(y_*)),$$
 (10a)

where

$$\bar{y}_* = k(x_*, X) \left[k(X, X) + \sigma_n^2 \mathbf{I} \right]^{-1} Y,$$
 (10b)

$$var(y_*) = k(x_*, x_*) - k(x_*, X) \left[k(X, X) + \sigma_n^2 \mathbf{I} \right]^{-1} k(X, x_*).$$
 (10c)

The true value of the modeled function may be approximated by the mean of the GP surrogate as given in Eq. (10b). The variance of the GP is a measure of the epistemic uncertainty of the model and can be used as an effective indicator

for where surrogate error may be reduced with additional samples. The gradient of the mean prediction at x_* can be obtained by differentiating Eq. (10b):

$$\nabla_{x}\bar{y}_{*} = \nabla_{x}k\left(x_{*}, X\right) \left(k(X, X) + \sigma_{n}^{2}\mathbf{I}\right)^{-1}Y.$$

For the radial basis function kernel in Eq. (9), the gradient is given by

$$\nabla_x k(x, x') = \frac{-\|x - x'\|}{l^2} \sigma_f^2 \exp\left(\frac{-\|x - x'\|^2}{2l^2}\right).$$

Higher derivatives can be computed by repeated differentiation of the kernel function. GP models in this work were generated using the scikit-learn Python library [34].

The mean prediction in Eq. (10b) can also be interpreted as the solution of a so-called optimal recovery problem in the theory of reproducing kernel Hilbert spaces (RKHS) [35, 36]. If \mathcal{H}_k , a Hilbert space of real scalar-valued functions in x, is the RKHS generated by the kernel k, then the solution of the smoothed interpolation problem

$$\min_{s \in \mathcal{H}_k} \ \frac{1}{2} \sum_{j=1}^m (s(x_j) - y_j)^2 + \frac{\sigma_n}{2} ||s||_{\mathcal{H}_k}^2$$

is given by [36, Thm. 7.11], [37, Sect. 2.3] as

$$s(x) = k(x, X) \left[k(X, X) + \sigma_n^2 \mathbf{I} \right]^{-1} Y.$$
 (11)

Moreover, if the observations $Y = [y_1, ..., y_N]^{\mathsf{T}}$ are evaluations of a function $f \in \mathcal{H}_k$, $y_j = f(x_j)$, j = 1, ..., N, then the pointwise error between the function and its smoothed interpolant given by Eq. (11) is bounded by

$$|s(x) - f(x)| \le \sqrt{k(x, x) - k(x, X) \left[k(X, X) + \sigma_n^2 \mathbf{I}\right]^{-1} k(X, x) + \sigma_n} \|f\|_{\mathcal{H}_{k + \sigma_n}},\tag{12}$$

where $\mathcal{H}_{k+\sigma_n}$ is the RKHS associated with the kernel $k+\sigma_n$. Note that $\mathcal{H}_{k+\sigma_n} \subset \mathcal{H}_k$ for all $\sigma_n \geq 0$ [35, Sect. 4.5], so $||f||_{\mathcal{H}_{k+\sigma_n}}$ is well-defined. Substituting Eqs. (10b) and (10c) into Eqs. (11) and (12) with $x=x_*$ gives

$$s(x_*) = \bar{y}_*,\tag{13a}$$

$$|\bar{y}_* - f(x_*)| \le \sqrt{\text{var}(y_*) + \sigma_n} \|f\|_{\mathcal{H}_{k+\sigma_n}}.$$
 (13b)

In other words, Eq. (13a) implies that the mean of a GP model for a scalar-valued function f constructed from samples at X yields a smoothed interpolant of f at X, and Eq. (13b) implies that the variance of the GP may be used to obtain a pointwise error bound between this interpolant and the true f. This error bound relies on the assumption that f lies in the RKHS generated by k; thus, a good choice of kernel is essential to the validity of the error bound when modeling general unknown functions. Techniques for kernel selection in GP regression are given in [37]. We use a simple RBF kernel in this work, but other kernels could be chosen provided they are twice continuously differentiable, such as the Matérn 5/2 kernel, sigmoid kernel, or polynomial kernels [10].

Illustrations of the lift and drag coefficient surrogates for a fixed design configuration are shown in Fig. 3 for N = 150 samples, which were generated using the Latin hypercube method. The GP fit is generally very good in the high-velocity regime, but underpredicts the aerodynamic coefficients at low velocities. This is likely due to a significant and nonlinear variation in performance at low supersonic speeds, making it challenging to model the full domain. A domain decomposition method, such as treed GPs [38, 39], might allow for more accurate prediction in this region.

Although not directly modeled by a surrogate, it is useful to consider the lift-to-drag ratio of the vehicle, which ultimately dictates glide efficiency and range. This can be found by elementwise division of corresponding C_L and C_D predictions. Results are plotted in Fig. 4 for two different numbers of samples. For a smaller number of samples, the surrogate becomes less refined in the low angle-of-attack range. Accuracy in the force coefficient surrogates is particularly important at low angle of attack since the small nominal drag values can significantly amplify errors when computing the lift-to-drag ratio.

An illustration of the surrogate for vehicle mass is given as a function of design parameters in Fig. 5. As with the aerodynamic surrogates, the domain bounds of sampled points are intentionally larger than the query bounds to ensure adequate coverage. Insufficient sampling on boundaries can lead to a poor-quality GP and result in the optimizer selecting an artificial local minimum.

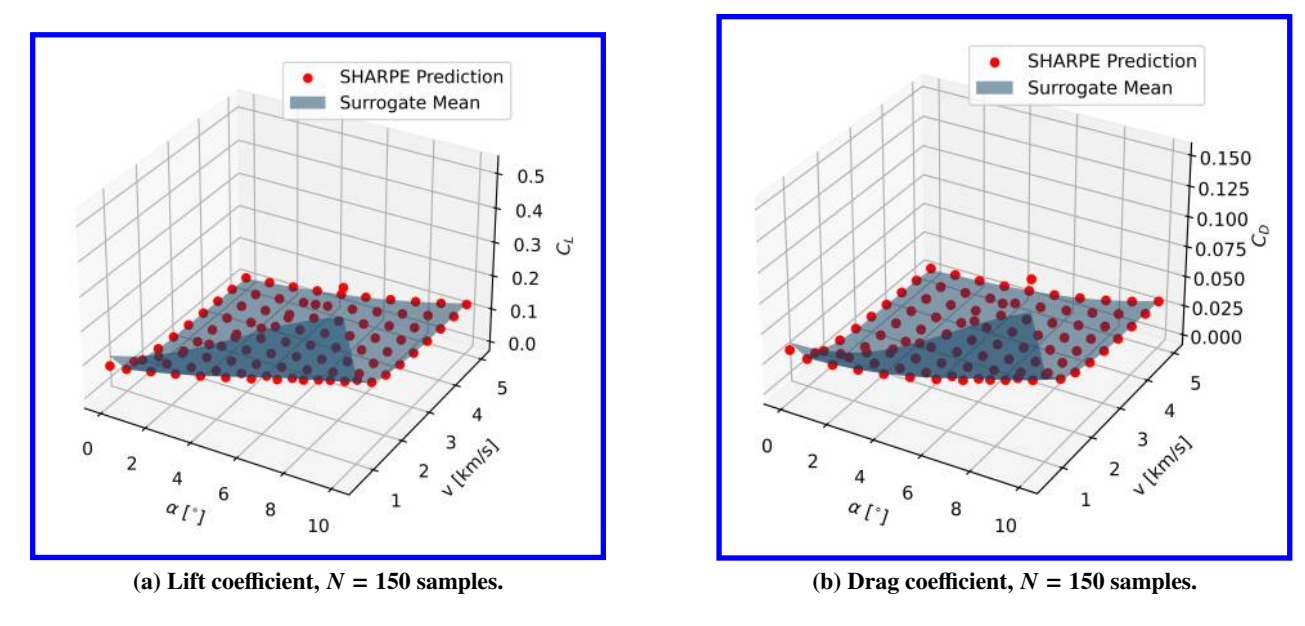


Fig. 3 Aerodynamic properties for vehicle configuration with $\theta = 3^{\circ}$ and $Ma_d = 12$.

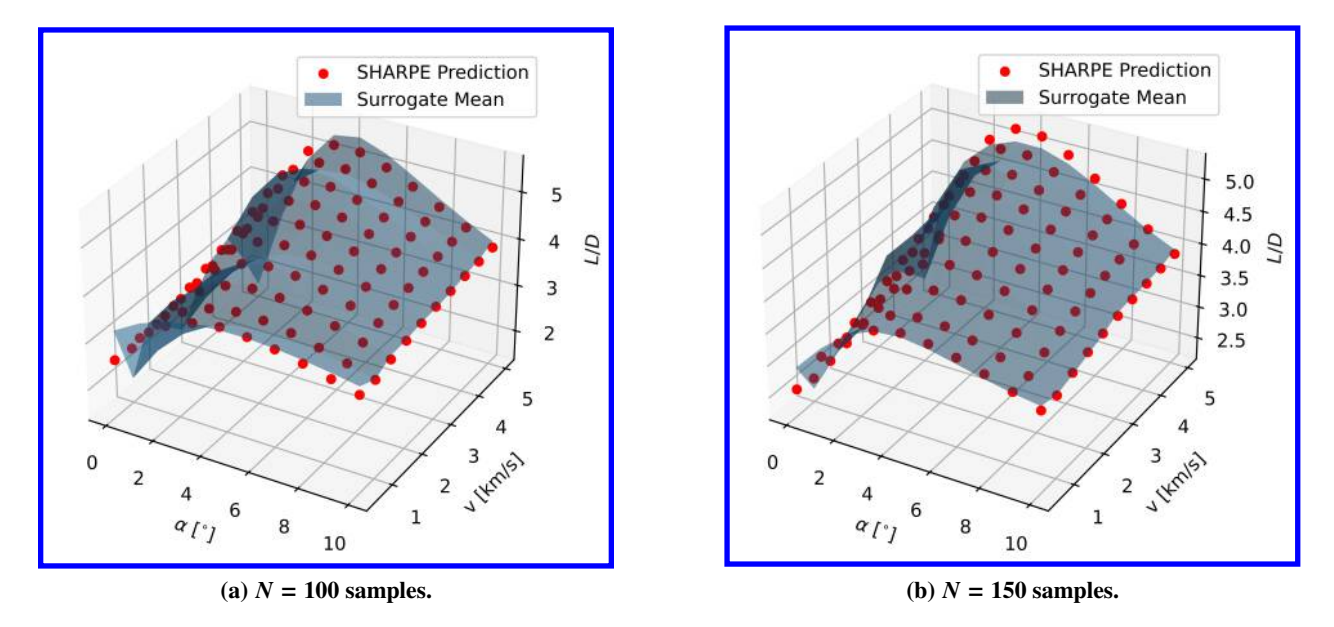


Fig. 4 Lift-to-drag ratio vs angle of attack and velocity for vehicle configuration with $\theta = 3^{\circ}$ and $Ma_d = 12$.

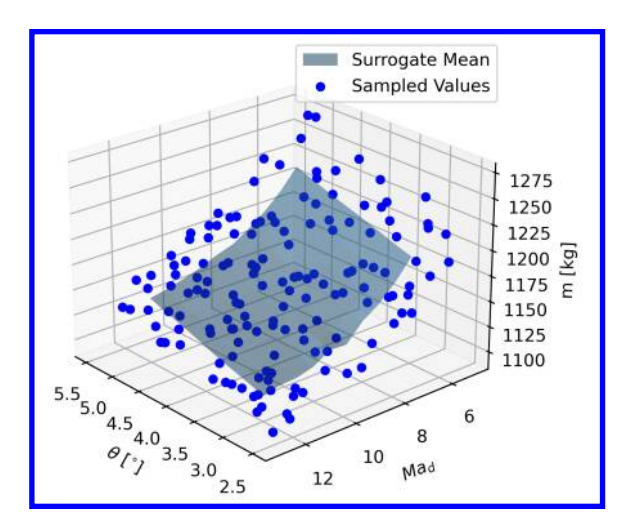


Fig. 5 Queried region of mass surrogate and sampled points.

V. Results

The specific co-design problem statement to implement and solve is a specific case of Eq. (2):

min
$$-x(t_f)$$

s.t. dynamics as in Eq. (7),
 $x(0) = 0$ km, $y(0) = 80$ km, $v(0) = 5$ km/s, $y(0) = -5^{\circ}$,
 $y(t_f) = 20$ km,
 $v(t) \ge 0.5$ km/s, $t \in [0, t_f]$, (14)
 $0^{\circ} \le \alpha(t) \le 10^{\circ}$, $t \in [0, t_f]$,
 $\bar{q}(y(t), v(t)) \le 40$ kPa, $t \in [0, t_f]$,
 $\dot{Q}_{\text{stag}}(y(t), v(t)) \le 8$ MW/m², $t \in [0, t_f]$,
 $\dot{Q}_{\text{stag}}(y(t), v(t)) \le 8$ MW/m², $t \in [0, t_f]$,

Based on experience with these types of vehicles and their typical structural and thermal designs, we selected 40 kPa and 8 MW/m² as upper limits for the dynamic pressure and the instantaneous heat flux that would not result in vehicle structural or TPS failure. Using tighter bounds resulted in the optimizer failing to find a feasible point. Additional studies on the consistency of these path constraints with various threshold values, as well as post-optimality sensitivity analysis of the resulting design and optimal trajectory, will be examined in future work.

The velocity is bounded above 0.5 km/s in Eq. (14) since we are primarily interested in the high-speed performance of the vehicle and the aerodynamic models in SHARPE are not sufficiently accurate at velocities below 0.5 km/s. Furthermore, at 0 km altitude, a terminal velocity of 0.5 km/s yields a dynamic pressure of approximately 153 kPa, which is much higher than the 40 kPa threshold; therefore, to make the problem feasible, the terminal altitude was set at 20 km, which yields a dynamic pressure of 9.3 kPa at a terminal velocity of 0.5 km/s. In principle, this problem may easily be reformulated with a much lower velocity bound and terminal altitude if reliable data is available for aerodynamic coefficients at low velocity.

The surrogate model $\hat{\mathbf{p}}$ is used to model vehicle aerodynamic properties over the joint state-control-parameter space, particularly the lift and drag coefficients C_L , C_D as well as the vehicle mass m. We constructed $\hat{\mathbf{p}}$ as a set of GP models employing RBF kernels with hyperparameters tuned by maximum likelihood estimation, using the Latin hypercube method to select sample locations in the region

$$v \in [0.4, 5.1], \ \alpha \in [-1^{\circ}, 11^{\circ}], \ Ma_d \in [5, 13], \ \theta \in [2.5^{\circ}, 5.5^{\circ}]$$

for evaluation of the high-fidelity model \mathbf{p}_* : $(v, \alpha, Ma_d, \theta) \to (C_L, C_D, m)$ given by the SHARPE package. Since the mass GP depends only on Ma_d and θ according to Eq. (4), the v and α values are ignored in the construction of the mass GP.

In all cases, we applied the Radau collocation method described in Sect. II to discretize the co-design problem in Eq. (14) using 80 equispaced subintervals of the time horizon with 3 collocation points per subinterval, and the primal-dual interior point solver Ipopt was used to solve the resulting NLP. Physical quantities were stored in units of km / kg / s for the optimization rather than the standard MKS system, as such choice resulted in better scaling of the problem and, therefore, more consistent optimizer performance.

A. Trajectory Co-Design

In our first computational experiment, we computed GP surrogates with N=150 Latin hypercube samples for use in solving Eq. (14). The initial iterate for the optimization solver Ipopt was constructed by following three steps. First, we fixed the vehicle parameters $Ma_d=9$, $\theta=4^\circ$ and used the angle of attack that yields the maximum lift-drag ratio as our initial control and simulated the dynamics in Eq. (7) using RK45 to compute a corresponding initial state. Second, the resulting trajectory was used as an initial guess for the solution of the fixed-vehicle-parameter trajectory optimization problem without the dynamic pressure and stagnation heating path constraints. This initialization strategy is motivated by the fact that maximizing the lift-drag ratio results in near-maximal downrange [40]. The optimal solution of this trajectory optimization problem was then used to initialize the same trajectory optimization problem with path constraints. Third, the optimal solution of this fixed-vehicle-parameter, path-constrained trajectory optimization problem was used to initialize Ipopt for the solution of Eq. (14).

Fig. 6 shows the optimal trajectory and control profile obtained for Eq. (14). The optimal vehicle parameters were $Ma_d = 12$, $\theta = 3^\circ$, which gave about a 300 km improvement in downrange over the initial guess of $Ma_d = 9$, $\theta = 4^\circ$. The trajectory plot in Fig. 6 also shows the optimal trajectory for fixed vehicle parameters $Ma_d = 9$, $\theta = 4^\circ$ (orange dashed line). We observe three distinct phases in the optimal trajectory: first, an initial dive at a high angle of attack to reduce dynamic pressure and stagnation heating, followed by a glide phase where the vehicle closely tracks the maximum lift-to-drag ratio, then ending with a brief descent phase at 0.5 km/s terminal velocity. Both dynamic pressure and stagnation heating reached peak values during the initial dive-pull maneuver, with the dynamic pressure constraint becoming active.

Figs. 7 and 8 show the differences between the initial vehicle geometry with $Ma_d = 9$, $\theta = 4^{\circ}$ and the optimal vehicle geometry with $Ma_d = 12$, $\theta = 3^{\circ}$.

B. Sensitivity to Surrogate Quality

The results in Sect. V.A were obtained using a fixed GP surrogate $\hat{\mathbf{p}}$ obtained from N=150 randomly generated samples. However, the quality of the optimal vehicle design and trajectory computed using optimization with surrogates depends on the quality of the surrogate model, and this dependency must be analyzed. In this study, we iteratively refine the surrogate model $\hat{\mathbf{p}}$ using additional samples of the high-fidelity model \mathbf{p}_* . Intuitively, as the model is successively refined, the optimal solution of Eq. (2) with $\hat{\mathbf{p}}$ should approach an optimal solution of Eq. (2) with the high-fidelity model \mathbf{p}_* . Specific model refinement procedures and their theoretical justification will be considered in future research.

To motivate the need for further research in this direction, we solved Eq. (14) using a simplistic model refinement strategy. First, we solved Eq. (14) using GP models generated with N = 125 Latin hypercube samples to obtain optimal vehicle parameters and an optimal trajectory. Initial iterates for the optimization algorithm were computed as discussed in Sect. V.A. Next, the GP models were refined using additional samples, which were generated using the current optimal values of the vehicle parameters Ma_d and θ , velocity v, and angle of attack α as follows. We selected 30 equispaced times t_1, \ldots, t_{30} in $[0, t_f]$, then queried the optimal trajectory at these times to obtain candidate sample locations

$$[v(t_i), \alpha(t_i), Ma_d, \theta]^\top, \quad i = 1, \dots, 30,$$

then we selected the 15 samples among those 30 for which $var(C_L) + var(C_D)$ was the largest, where $var(C_L)$ and $var(C_D)$ denote the variance of the GPs for lift and drag coefficients evaluated at the candidate sample locations in Eq. (15). The use of $var(C_L) + var(C_D)$ as an error indicator for the GPs is motivated by the bound in Eq. (13b). These 15 samples were added to the GP models and Eq. (14) was resolved with the refined models, using the solution obtained from the previous model as the initial guess for the optimizer. This process was repeated until the optimizer failed to find a solution. For demonstration purposes, in contrast to Sect. V.A, the initial GP models were constructed using N = 125 Latin hypercube samples rather than N = 150, leading to undersampling in some regions of the domain. As the models were refined, the undersampling effects quickly faded, and the quality of the solution steadily improved.

The optimal solutions of Eq. (14) for successive model refinements are compared in Fig. 9, with optimal vehicle parameters given in Table 2. We use the notation N = 125 + 15(r) to indicate that r refinements were used, each

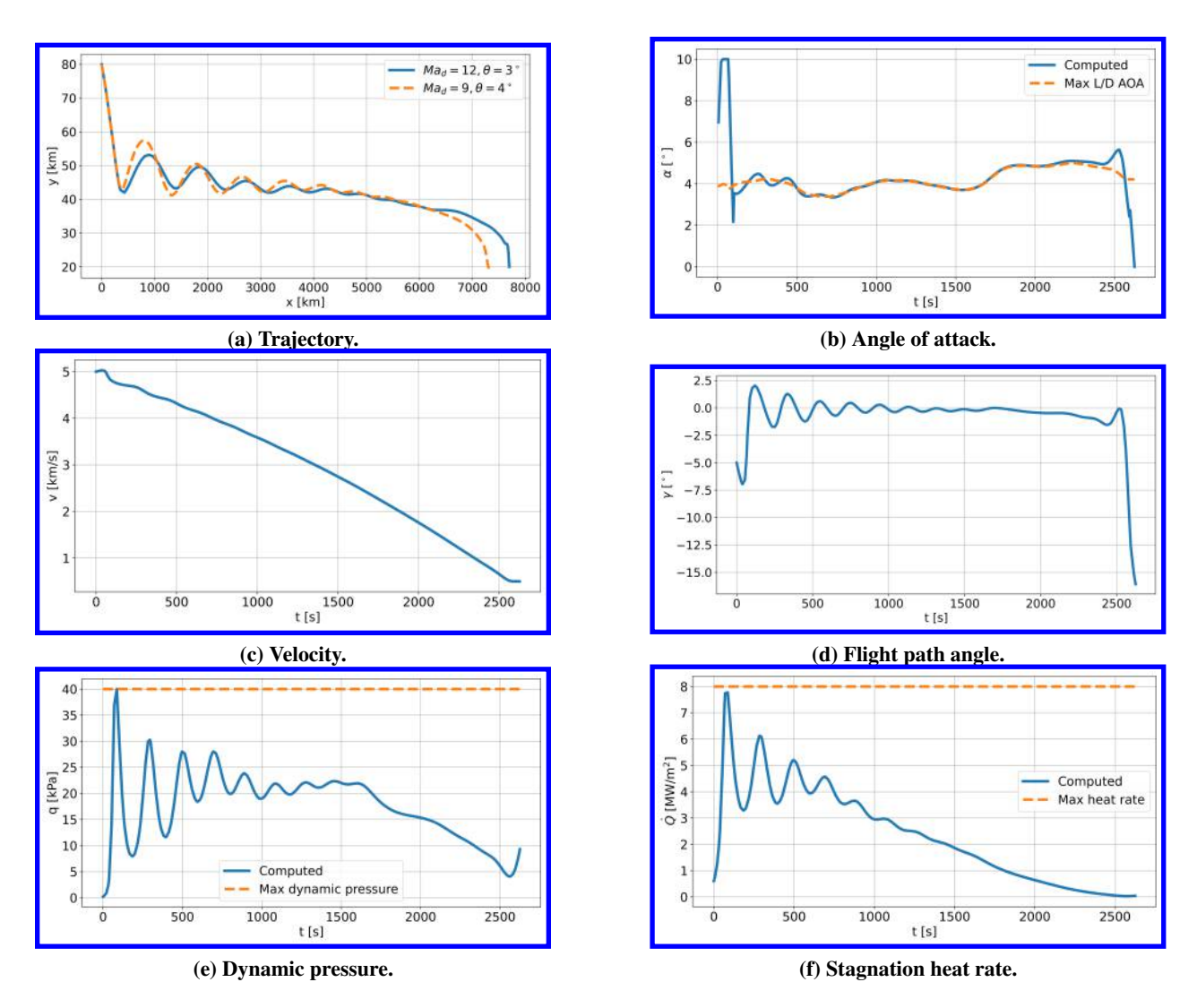
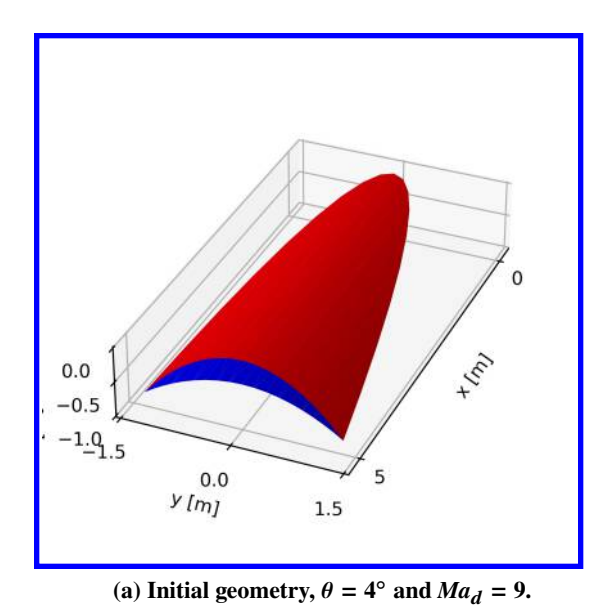
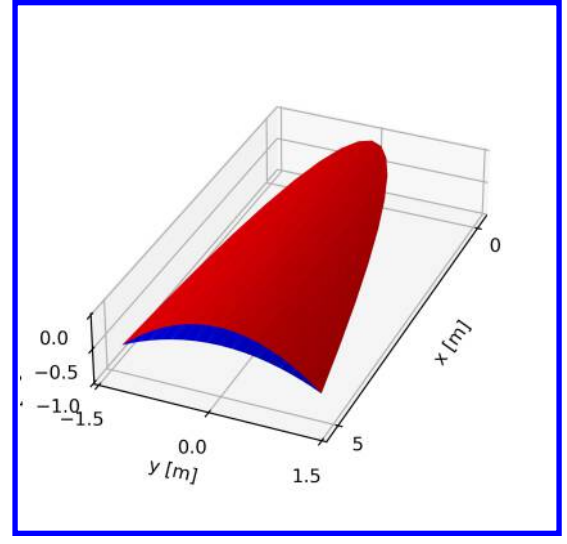


Fig. 6 Optimal solution of co-design problem with GP models obtained from N = 150 Latin hypercube samples.

time adding 15 samples using the aforementioned scheme. We show the results after 6 successive refinements. The samples became too clustered after the 7th refinement, causing issues with hyperparameter tuning and resulting in Ipopt failing to converge. The velocity and angle-of-attack samples used for GP computation and refinement are shown in Fig. 10. The particular samples added to each model are color-coded in correspondence with the color-coding of the optimal trajectories in Fig. 9. For example, the yellow trajectory in Fig. 9 was obtained by solving Eq. (14) with the N = 125 + 15(2) surrogate, which was constructed using the dark red, light blue, and yellow samples in Fig. 10.

We observe that as the models are refined, the optimal trajectories, control profiles, and vehicle parameters appear to converge, as the last three trajectories are neatly stacked on top of one another. As a consequence, the samples added to the GP models begin to cluster around this limit, and adding too many samples eventually leads to overfitting and poor optimizer performance. These results indicate that suitable refinement of GP models can lead to vehicle parameters and trajectories that are close to the optimal vehicle parameters and trajectories corresponding to the high fidelity model \mathbf{p}_* . However, better refinement strategies are needed and theoretical convergence guarantees are still missing. In this setting, we used the GP variance, i.e., $var(C_L) + var(C_D)$, as an indicator for the error between the current surrogate and the high-fidelity model. This heuristic was observed to yield a good reduction in error of the current GP model at the current solution, and it tended to add samples in high-uncertainty regions farther away from previous samples, preventing numerical issues with GP model computation and associated numerical issues with the optimization algorithm. However, it may be more advantageous to use optimality-based sensitivity analysis to sample





(b) Optimal geometry, $\theta = 3^{\circ}$ and $Ma_d = 12$.

Fig. 7 Comparison of initial and optimized configurations for N = 150 samples.

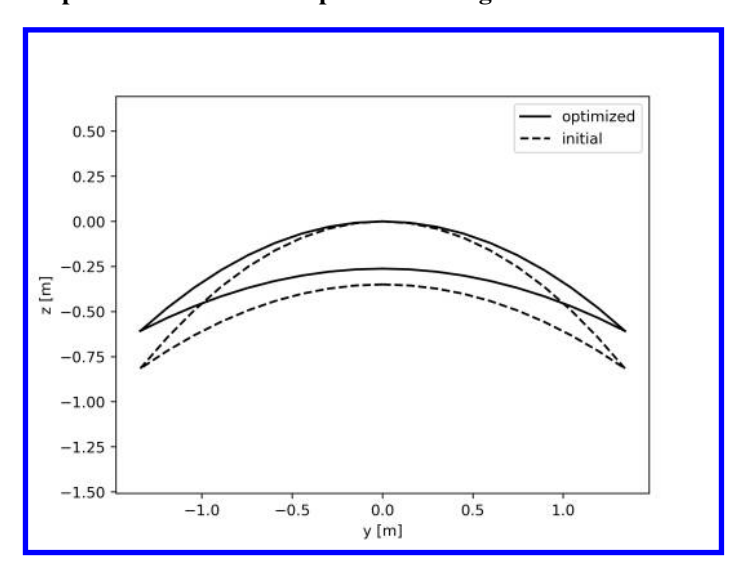


Fig. 8 Comparison of initial and optimized rear surface profiles.

No. of samples	Ma_d	θ
N = 125 + 15(0)	7.11	5.00°
N = 125 + 15(1)	12.00	3.00°
N = 125 + 15(2)	12.00	4.03°
N = 125 + 15(3)	12.00	3.00°
N = 125 + 15(4)	12.00	3.00°
N = 125 + 15(5)	12.00	3.07°
N = 125 + 15(6)	12.00	3.00°

Table 2 Optimal vehicle design parameters for co-design problem with successive model refinements.

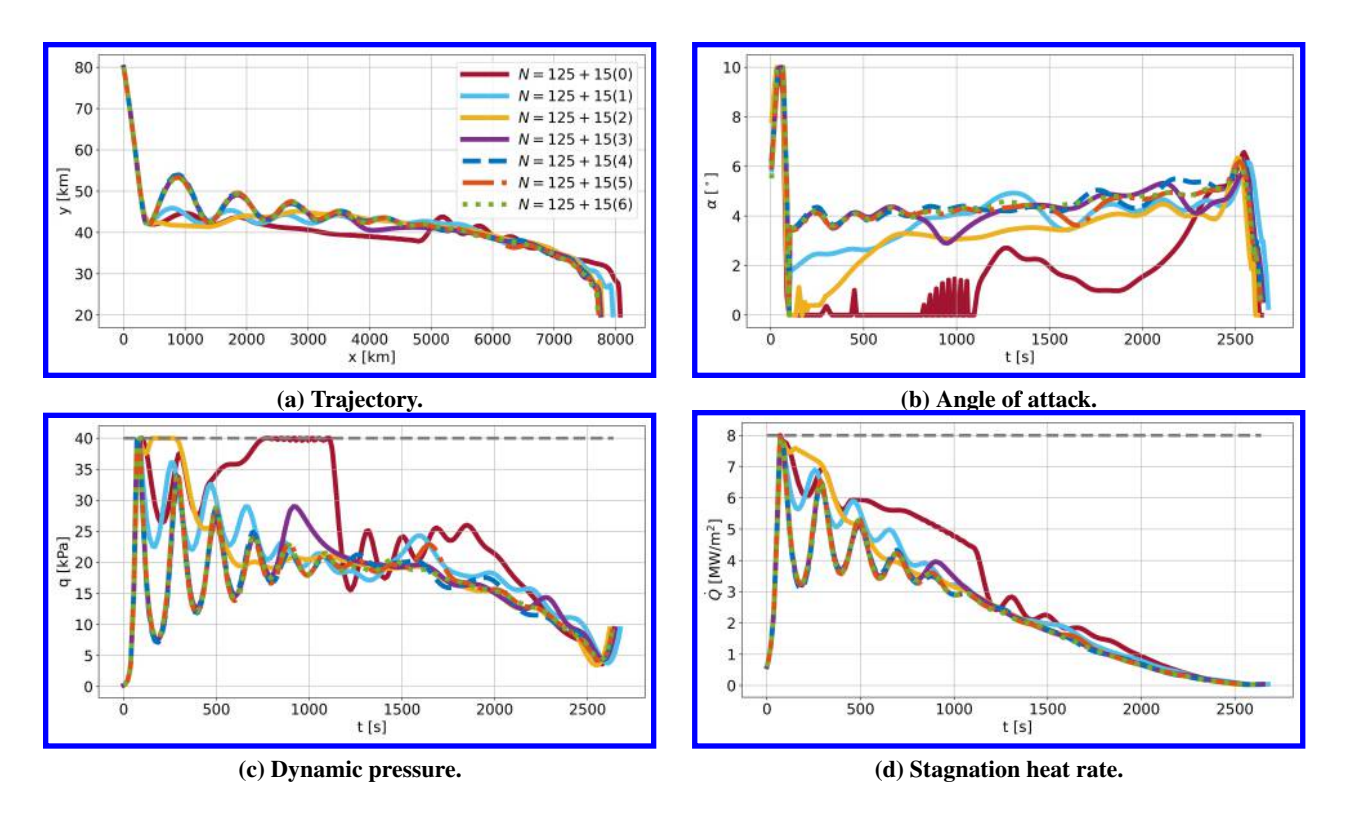


Fig. 9 Optimal solutions for co-design problem with successive model refinements.

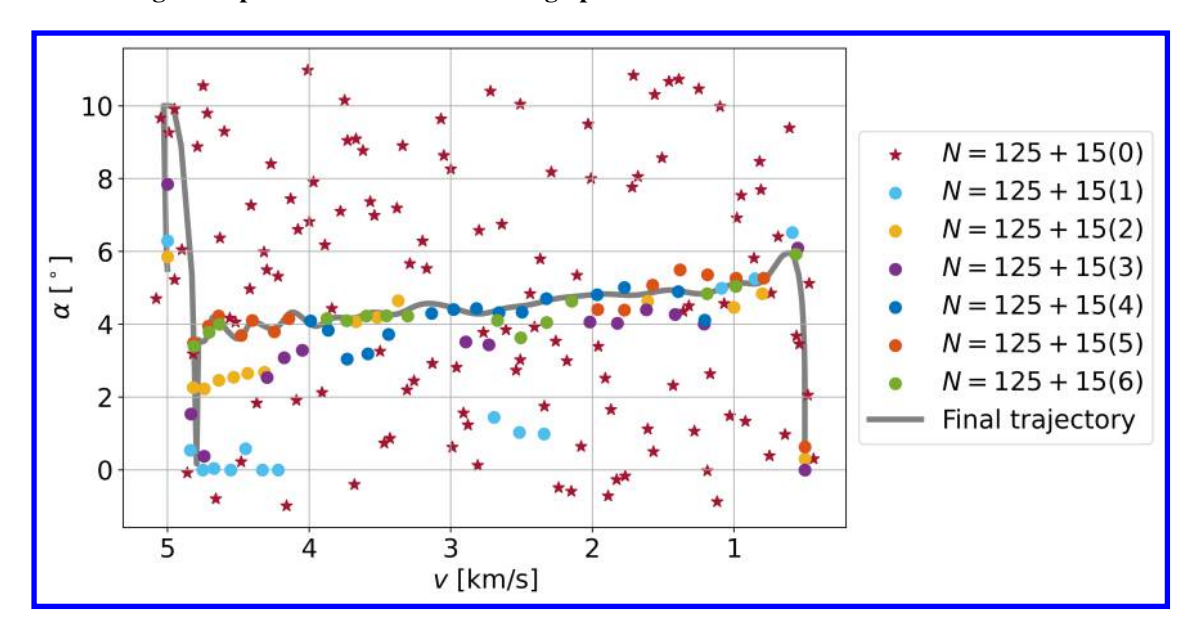


Fig. 10 GP sample locations (velocity and angle of attack only) used in successive model refinements.

where errors in the current GP most impact the current optimal solution. Moreover, adding a fixed number of samples along each optimal trajectory is rather naive. If the vehicle parameters and optimal trajectories converge, adding a fixed number of samples will eventually force additional samples to be taken near current ones and cause numerical issues even when selecting for maximum uncertainty, as we observed in our experiments. Accordingly, the selection of additional samples must balance error reduction and numerical properties of the resulting GP. For example, we chose to compute $var(C_L) + var(C_D)$ at the 30 samples indicated by Eq. (15) and select the 15 samples corresponding to the largest $var(C_L) + var(C_D)$ to refine our GP models. If instead we had used, e.g., 50 (or more) candidate samples

in Eq. (15), then likely some of the 15 samples corresponding to the largest $var(C_L) + var(C_D)$ would have been too tightly packed, leading to numerical issues in the GP refinement and consequently in the optimization. When using 50 candidate samples for refinements instead of 30, we did indeed observe this outcome, as the optimizer was unable to find a solution after a single refinement. Selecting 15 samples from 30 candidates gave satisfactory results in this study, but more rigorous, problem-independent, optimization-based sampling approaches will be considered in future research.

VI. Conclusion

This manuscript described a methodology for simultaneous vehicle and trajectory optimization of a hypersonic glide vehicle. The co-design task was formulated as a single constrained optimization problem, which was discretized using the Radau collocation method and solved simultaneously in the vehicle design parameters, the discretized states, and the discretized controls. Vehicle mass and aerodynamic performance were modeled using a set of GP surrogates which were directly integrated into the optimization procedure. The use of GP surrogates provided computationally efficient evaluations of vehicle mass and aerodynamic performance surrogates as well as their (analytical) first- and second-order derivatives, which benefited the application of the simultaneous solution approach and the use of efficient derivative-based optimization algorithms.

A test problem was run for conditions similar to a boosted hypersonic glide vehicle mission profile, demonstrating the capability of the procedure to generate an optimal vehicle design and trajectory while satisfying problem constraints. Additionally, a basic approach to surrogate refinement was proposed in this paper to mitigate the effects of surrogate error on the optimal solution. The results demonstrate that this surrogate refinement can significantly improve the quality of the optimal solution. Moreover, in our computations the optimal vehicle parameters and trajectories appeared to converge as the surrogates were refined. However, our basic refinement strategy eventually suffers from overfitting, numerical instability, and related numerical issues in the optimization if too many samples are added. Currently, the number of samples added and the number of surrogate refinement steps are determined manually.

Several avenues exist for future work. One such area is increasing the number of design variables in the optimization problem. Particularly, including the effect of altitude on aerodynamics, as well as incorporating models for important aerodynamic phenomena such as turbulent transition, will permit more accurate prediction of flow properties in the low-altitude segment of the trajectory. Additionally, increasing the number of design variables for a more complex vehicle geometry would permit greater design freedom. There is also the improvement of integration between disciplinary models, including coupling vehicle weight estimation with TPS sizing and structural analysis models, which would permit a more accurate comparison between candidate trajectories and designs.

An attractive feature of GP surrogate models is the capability to incorporate multi-fidelity data. This has previously been demonstrated for the generation of aerodynamic databases [41] and would permit the inclusion of high-fidelity model data (e.g., computational fluid dynamics simulations) to improve surrogate predictions in critical regions of the design space where data from low-fidelity methods may be inaccurate or carry high uncertainty. While the methodology described in this manuscript has been developed and applied to GP surrogates, it could also be extended to other surrogate modeling techniques, such as projection-based reduced order models, provided the necessary derivative information can be computed.

On the theoretical side, future work will also focus on a better understanding of the impact of surrogate quality on the optimal solution as well as a better understanding of existing automated refinement procedures and their convergence guarantees. The dependence of the solution on surrogate quality also motivates the development of sensitivity-driven model refinement techniques to adaptively select sample points that will most improve the resulting solution when integrated into the models. Finally, we currently assume that the samples used to generate the GPs are computed from a high-fidelity model. Incorporating multi-fidelity models would provide opportunities to further reduce sampling costs by computing sample points for surrogates at appropriate levels of fidelity depending on the sensitivity of the optimal trajectory to model discrepancies at those sample locations.

Acknowledgments

This work was supported by the Air Force Office of Scientific Research under Grant FA9550-22-1-0004.

References

[1] Bowcutt, K. G., "Physics Drivers of Hypersonic Vehicle Design," Paper AIAA 2018-5373. 22nd AIAA International Space Planes and Hypersonics Systems and Technologies Conference, 2018. https://doi.org/10.2514/6.2018-5373, URL

- https://doi.org/10.2514/6.2018-5373.
- [2] Sayler, K. M., "Hypersonic Weapons: Background and Issues for Congress," Tech. Rep. CRS Report R45811, Congressional Research Service, 2023. URL https://crsreports.congress.gov/product/pdf/R/R45811.
- [3] Rizvi, S. T., Linshu, H., Dajun, X., and Shah, S. I., "Trajectory Optimisation for a Rocket-Assisted Hypersonic Boost-Glide Vehicle," *Aeronautical Journal*, Vol. 121, 2017, pp. 469–487. https://doi.org/10.1017/aer.2017.11.
- [4] Zhang, G., He, J., and Vlahopoulos, N., "Multidisciplinary Design under Uncertainty for a Hypersonic Vehicle," 13th AIAA/ISSMO Multidisciplinary Analysis Optimization Conference, Paper AIAA 2010-9189, 2010. https://doi.org/10.2514/6.2010-9189, URL https://doi.org/10.2514/6.2010-9189.
- [5] Armellin, R., Lavagna, M., Starkey, R. P., and Lewis, M. J., "Aero-Gravity Assist Maneuvers: Coupled Trajectory and Vehicle Shape Optimization," *Paper AIAA 2006-6036. AIAA/AAS Astrodynamics Specialist Conference and Exhibit. August 2006*, 2006. https://doi.org/10.2514/6.2006-6036, URL https://doi.org/10.2514/6.2006-6036.
- [6] Makkapati, V. R., Ridderhof, J., Tsiotras, P., Hart, J., and van Bloemen Waanders, B., "Desensitized Trajectory Optimization for Hypersonic Vehicles," 2021 IEEE Aerospace Conference (50100), 2021, pp. 1–10. https://doi.org/10.1109/AERO50100.2021. 9438511, URL http://dx.doi.org/10.1109/AERO50100.2021.9438511.
- [7] Seywald, H., and Seywald, K. L., "Desensitized Optimal Control," AIAA Scitech 2019 Forum, 2019. https://doi.org/10.2514/6. 2019-0651, URL https://doi.org/10.2514/6.2019-0651.
- [8] Hart, J., van Bloemen Waanders, B., Hood, L., and Parish, J., "Sensitivity-Driven Experimental Design to Facilitate Control of Dynamical Systems," J. Optim. Theory Appl., Vol. 196, No. 3, 2023, pp. 855–881. https://doi.org/10.1007/s10957-023-02172-w, URL https://doi.org/10.1007/s10957-023-02172-w.
- [9] Bowcutt, K., Kuruvila, G., Grandine, T., and Cramer, E., "Advancements in Multidisciplinary Design Optimization Applied to Hypersonic Vehicles to Achieve Performance Closure," 15th AIAA International Space Planes and Hypersonic Systems and Technologies Conference, American Institute of Aeronautics and Astronautics, 2008. https://doi.org/10.2514/6.2008-2591, URL https://arc.aiaa.org/doi/10.2514/6.2008-2591.
- [10] Rasmussen, C. E., and Williams, C. K. I., Gaussian Processes for Machine Learning, MIT Press, 2006.
- [11] Nakka, S. K. S., and Alexander-Ramos, M. J., "Simultaneous Combined Optimal Design and Control Formulation for Aircraft Hybrid-Electric Propulsion Systems," *Journal of Aircraft*, Vol. 58, 2021, pp. 53–62. https://doi.org/10.2514/1.C035678.
- [12] Allison, J. T., and Herber, D. R., "Multidisciplinary Design Optimization of Dynamic Engineering Systems," *AIAA Journal*, Vol. 52, 2014, pp. 691–710. https://doi.org/10.2514/1.J052182, URL https://doi.org/10.2514/1.J052182.
- [13] Stryk, O. V., and Bulirsch, R., "Direct and Indirect Methods for Trajectory Optimization," Annals of Operations Research, Vol. 37, 1992, pp. 357–373. https://doi.org/10.1007/BF02071065, URL https://doi.org/10.1007/BF02071065.
- [14] Betts, J. T., Practical Methods for Optimal Control Using Nonlinear Programming, 3rd ed., Advances in Design and Control, Vol. 36, Society for Industrial and Applied Mathematics (SIAM), Philadelphia, PA, 2020. https://doi.org/10.1137/1. 9781611976199, URL https://doi.org/10.1137/1.9781611976199.
- [15] Biegler, L. T., Nonlinear Programming. Concepts, Algorithms, and Applications to Chemical Processes, MOS-SIAM Series on Optimization, Vol. 10, Society for Industrial and Applied Mathematics (SIAM), Philadelphia, PA, 2010. https://doi.org/10.1137/1.9780898719383, URL https://doi.org/10.1137/1.9780898719383.
- [16] Kameswaran, S., and Biegler, L. T., "Convergence Rates for Direct Transcription of Optimal Control Problems using Collocation at Radau Points," Comput. Optim. Appl., Vol. 41, No. 1, 2008, pp. 81–126. https://doi.org/10.1007/s10589-007-9098-9, URL http://doi.org/10.1007/s10589-007-9098-9.
- [17] Hager, W. W., Hou, H., Mohapatra, S., Rao, A. V., and Wang, X.-S., "Convergence Rate for a Radau hp Collocation Method Applied to Constrained Optimal Control," *Comput. Optim. Appl.*, Vol. 74, No. 1, 2019, pp. 275–314. https://doi.org/10.1007/s10589-019-00100-1.
- [18] Garg, D., Patterson, M., Hager, W. W., Rao, A. V., Benson, D. A., and Huntington, G. T., "A Unified Framework for the Numerical Solution of Optimal Control Problems using Pseudospectral Methods," *Automatica J. IFAC*, Vol. 46, No. 11, 2010, pp. 1843–1851. https://doi.org/10.1016/j.automatica.2010.06.048, URL http://dx.doi.org/10.1016/j.automatica.2010.06.048.

- [19] Kameswaran, S., and Biegler, L. T., "Advantages of Nonlinear-Programming-Based Methodologies for Inequality Path-Constrained Optimal Control Problems—A Numerical Study," SIAM J. Sci. Comput., Vol. 30, No. 2, 2008, pp. 957–981. https://doi.org/10.1137/050644938, URL http://doi.org/10.1137/050644938.
- [20] Wächter, A., and Biegler, L., "On the implementation of an interior-point filter line-search algorithm for large-scale nonlinear programming," *Math. Program.*, Vol. 106, No. 1, Ser. A, 2006, pp. 25–57. https://doi.org/10.1007/s10107-004-0559-y, URL https://doi.org/10.1007/s10107-004-0559-y.
- [21] Griewank, A., and Walther, A., Evaluating Derivatives. Principles and Techniques of Algorithmic Differentiation, 2nd ed., Society for Industrial and Applied Mathematics (SIAM), Philadelphia, PA, 2008. https://doi.org/10.1137/1.9780898717761, URL https://doi.org/10.1137/1.9780898717761.
- [22] Starkey, R. P., and Lewis, M. J., "Simple Analytical Model for Parametric Studies of Hypersonic Waveriders," *Journal of Spacecraft and Rockets*, Vol. 36, 1999, pp. 516–523. https://doi.org/10.2514/3.27194.
- [23] Needels, J. T., and Alonso, J. J., "Efficient Global Optimization for Multidisciplinary Conceptual Design of Hypersonic Vehicles," AIAA Aviation 2023 Forum, American Institute of Aeronautics and Astronautics Inc., 2023. URL https://doi.org/10.2514/6.2023-3718.
- [24] White, F., Viscous Fluid Flow, McGraw-Hill, 2006.
- [25] Marley, C. D., and Driscoll, J. F., "Modeling an Active and Passive Thermal Protection System for a Hypersonic Vehicle," AIAA SciTech Forum - 55th AIAA Aerospace Sciences Meeting, American Institute of Aeronautics and Astronautics Inc., 2017. https://doi.org/10.2514/6.2017-0118.
- [26] Sutherland, W., "The Viscosity of Gases and Molecular Force," The London, Edinburgh, and Dublin Philosophical Magazine and Journal of Science, Vol. 36, 1893, pp. 507–531. https://doi.org/10.1080/14786449308620508.
- [27] Bertin, J. J., and Cummings, R. M., "Critical Hypersonic Aerothermodynamic Phenomena," *Annual Review of Fluid Mechanics*, Vol. 38, 2006, pp. 129–157. https://doi.org/10.1146/annurev.fluid.38.050304.092041.
- [28] Urzay, J., and Renzo, D. M. D., "Engineering Aspects of Hypersonic Turbulent Flows at Suborbital Enthalpies," Center for Turbulence Research Annual Research Briefs, 2020.
- [29] Williams, S. D., and Curry, D. M., "NASA Reference Publication 1289: Thermal Protection Materials Thermophysical Property Data," Tech. rep., National Aeronautics and Space Administration, 1992.
- [30] "AETB-12 Rigid Tile," TPSX NASA Material Property Database, 2001. URL https://tpsx.arc.nasa.gov/Material?id=6.
- [31] "Aluminum 2024-T4; 2024-T351," ASM Matweb, 2023. URL https://asm.matweb.com/search/SpecificMaterial.asp?bassnum=ma2024t4.
- [32] Rizvi, S. T. I., He, L., and Xu, D., "Optimal Trajectory Analysis of Hypersonic Boost-Glide Waverider with Heat Load Constraint," Aircraft Engineering and Aerospace Technology, Vol. 87, No. 1, 2015, pp. 67–78. https://doi.org/10.1108/AEAT-04-2013-0079, URL https://doi.org/10.1108/AEAT-04-2013-0079.
- [33] Tauber, M. E., "NASA Technical Paper 2914: A Review of High-Speed, Convective, Heat-Transfer Computation Methods," Tech. rep., National Aeronautics and Space Administration, 1989.
- [34] Pedregosa, F., et al., "Scikit-learn: Machine Learning in Python," Journal of Machine Learning Research, Vol. 12, 2011, pp. 2825–2830.
- [35] Berlinet, A., and Thomas-Agnan, C., Reproducing Kernel Hilbert Spaces in Probability and Statistics, Kluwer Academic Publishers, Boston, MA, 2004. https://doi.org/10.1007/978-1-4419-9096-9, URL https://doi.org/10.1007/978-1-4419-9096-9, with a preface by Persi Diaconis.
- [36] Schaback, R., and Wendland, H., "Kernel Techniques: From Machine Learning to Meshless Methods," Acta Numerica, 2006, Acta Numer., Vol. 15, Cambridge Univ. Press, Cambridge, 2006, pp. 543–639. https://doi.org/10.1017/S0962492906270016, URL https://doi.org/10.1017/S0962492906270016.
- [37] Akian, J.-L., Bonnet, L., Owhadi, H., and Savin, E., "Learning "Best" Kernels from Data in Gaussian Process Regression. With application to aerodynamics," J. Comput. Phys., Vol. 470, 2022, p. Paper No. 111595. https://doi.org/10.1016/j.jcp.2022.111595, URL https://doi.org/10.1016/j.jcp.2022.111595.

- [38] Gramacy, R. B., and Lee, H. K., "Bayesian Treed Gaussian Process Models with an Application to Computer Modeling," Journal of the American Statistical Association, Vol. 103, 2008, pp. 1119–1130. https://doi.org/10.1198/016214508000000689.
- [39] Nelson, A. J., "Treed Kriging Aerodynamic Database Modeling and Optimization," Ph.D. thesis, Stanford University, 2008.
- [40] Yu, W., and Chen, W., "Guidance Scheme for Glide Range Maximization of a Hypersonic Vehicle," *AIAA Guidance, Navigation, and Control Conference, 8-11 August 2011, Portland, Oregon, Paper AIAA 2011-6714*, 2011. https://doi.org/10.2514/6.2011-6714, URL https://doi.org/10.2514/6.2011-6714.
- [41] Wendorff, A. D., Alonso, J. J., Bieniawski, S. R., and Whitehead, B. T., "Integrating Aerodynamic Uncertainty into Aircraft Maneuvers During Conceptual Design," *Paper AIAA 2016-3999. 17th AIAA/ISSMO Multidisciplinary Analysis and Optimization Conference*, 2016. https://doi.org/10.2514/6.2016-3999, URL https://doi.org/10.2514/6.2016-3999.